Nanoscale



PAPER

View Article Online
View Journal | View Issue



Cite this: *Nanoscale*, 2025, **17**, 23716

# Fabrication of flexible memristors using PMMA-rGO/Au nanocomposite thin films with improved stability and retention time

Shivam Awasthi,†[a] Subarna Pramanik, †[b] Rajarshi Chakraborty, [b] Anita Mohan[a] and Bhola Nath Pal *[b]

Flexible memristor devices with high retention capability and enhanced stability are fabricated using a cost-effective, low-temperature spin coating technique. The active switching layer of the device, composed of polymethyl methacrylate embedded reduced graphene oxide (rGO)/Au nanoparticle (NPs) heterostructure thin films, is sandwiched between an ITO-coated conducting PET substrate as the bottom electrode and thermally deposited aluminum top electrodes. Compared to the reference GO/PMMA device, this device exhibited remarkable enhancement in overall electrical performance. The operating voltages are limited to +1.4 V/−2.15 V, representative of the low power consumption of the device. The device also exhibited excellent endurance, maintaining stable operation for over 75 consecutive switching cycles and a high retention time of ~$2 \times 10^4$ s. The excellent stability of the device is attributed to the incorporation of Au nanoparticles within the graphene nanosheets, which improved the structural stability of the heterostructures by preventing the restacking of the nanosheets. Additionally, Au nanoparticles introduced localized electronic states, acting as active sites for charge storage and improving the overall conductivity. The nanoscale interactions between Au NP and graphene nanosheets reduced the energy barriers and contributed to improved charge mobility. Flexibility studies established a critical bending radius of 6 mm, and the device exhibited stable switching operation even after 1000 continuous bending cycles, establishing it as an excellent memory candidate for low-power flexible and portable electronics.

Received 27th June 2025,
Accepted 17th September 2025

DOI: 10.1039/d5nr02726h

rsc.li/nanoscale



## 1. Introduction

In recent years, the rapid advancements in artificial intelligence, neuromorphic computing, and data storage technologies have driven an urgent need for innovative memory devices.[1–3] Among these, memristors[4] have garnered immense attention as promising candidates for next-generation computing systems.[5–8] By mimicking the behavior of biological synapses, these non-volatile memory components can change their resistance under an applied electric field, enabling efficient data storage and processing.[9–12] With their advantages of low energy consumption and high storage density, memristors hold great potential for transforming how data are managed in modern electronics.[13,14]

Despite these advantages, several challenges remain. Mechanical flexibility, high endurance, and long-term stability are key barriers preventing the widespread adoption of memristors, especially in emerging applications like wearable electronics and flexible computing devices. Traditional memristors, commonly fabricated from materials such as metal oxides, organic compounds, or chalcogenides, face inherent trade-offs. Oxide materials have recently attracted significant attention for their ease of use, environmental stability, and versatile applications in fields like memristors, photoconductors, phototransistors, and smart windows.[15–18] For example, oxide-based memristors, like those made from $TiO_2$ or $HfO_2$, offer an excellent switching speed and data retention but lack mechanical flexibility, making them prone to failure under mechanical stress.[19–25] On the other hand, organic memristors are more adaptable to bending and stretching but often suffer from poor thermal and environmental stability. These limitations highlight the critical need for new materials and device architectures that can simultaneously achieve flexibility, durability, and reliable performance.[26,27]

To address these issues, researchers have increasingly turned to hybrid materials that combine flexibility with enhanced durability.[28–30] Among these, graphene stands out as a particularly attractive candidate due to its exceptional elec-

[a]*Department of Physics, Indian Institute of Technology (BHU), Varanasi-221005, UP, India*
[b]*School of Materials Science and Technology, Indian Institute of Technology (BHU), Varanasi 221005, UP, India. E-mail: bnpal.mst@iitbhu.ac.in*
†The authors have contributed equally.

trical conductivity, mechanical flexibility, and chemical stability.[31] However, pristine graphene lacks the intrinsic resistive switching behavior required for memristive applications. One promising solution is to integrate graphene with nanoparticles such as gold (Au), forming heterostructures that facilitate resistive switching. Embedding these heterostructures in a polymethyl methacrylate (PMMA) matrix further enhances mechanical stability while providing a dielectric environment that improves operational performance.[32] Despite the potential of these hybrid systems, research on PMMA-embedded graphene/Au nanoparticle heterostructures for flexible memristors remains limited. For instance, Midya *et al.* developed an Au nanoparticle-reduced graphene oxide (rGO) hybrid in a polyvinyl alcohol (PVA) matrix using a one-pot synthesis method.[33] While their work demonstrated some promise, the resulting devices suffered from inadequate ON/OFF current ratios ($\sim 10^3$) and poor stability, as indicated by endurance characteristics of fewer than 25 cycles.

In this work, we introduce a flexible memristor device designed to overcome these limitations. By embedding a graphene and gold nanoparticle heterostructure within a PMMA matrix, we achieve a unique combination of mechanical flexibility, enhanced durability, and stable resistive switching performance. Unlike PVA, which is moisture-sensitive, PMMA offers superior environmental stability and higher dielectric strength, minimizing leakage currents and enhancing switching reliability. While PI provides excellent thermal stability and robustness, its rigidity limits flexibility. The PMMA matrix provides structural robustness and adaptability to mechanical stress, while the graphene/Au nanoparticle network ensures reliable resistive switching by facilitating the controlled formation and dissolution of conductive filaments. This novel approach not only addresses critical challenges in flexible memory devices but also offers a scalable, cost-effective solution for future electronics. The enhanced stability and functionality of this flexible memristor make it an ideal candidate for applications in wearable devices, soft robotics, and flexible displays, where reliability and adaptability are essential. By paving the way for durable and high-performing flexible memory systems, this work contributes to the broader vision of developing smart, adaptive electronics for diverse industries.

## 2. Experimental

### 2.1 Materials

Commercial graphite powder (<20 μm), sulphuric acid (98% purity), sodium nitrate (97% purity), potassium permanganate (98% purity), and hydrogen peroxide (analytical grade) are used for the synthesis of graphene oxide (GO), whereas hydrochloric acid (analytical grade), ethanol (99% purity), and DI water are used for the purification process of graphene oxide. Other chemicals used for PNC, like sodium borohydride (ACS reagent 99%), chloroauric acid (98% purity), isopropyl alcohol (99% purity), acetone (analytical grade), polymethyl methacrylate (average $M_w$ ~120 000 by GPC), ITO-coated PET substrate, and dimethyl formamide (ACS reagent 99%), are purchased from Sigma-Aldrich.

### 2.2 Synthesis methodology of rGO/Au heterostructures

The synthesis of reduced graphene oxide (rGO)/gold (Au) nanoparticle heterostructures has been performed using a hydrothermal synthesis method, with graphene oxide (GO) and chloroauric acid ($HAuCl_4$) serving as the precursors and sodium borohydride ($NaBH_4$) as the reducing agent. The graphene oxide is synthesized using a modified Hummers' method, yielding a brownish powder of GO. After drying, 50 mg of GO is dispersed in 50 mL of deionized water using ultrasonication for 1 h to obtain a stable colloidal dispersion. Separately, an aqueous solution of $HAuCl_4{\cdot}3H_2O$ is prepared by adding 50 mg of $HAuCl_4{\cdot}3H_2O$ to 20 mL of deionized water, followed byultrasonication for 1 h, yielding a concentration of ~6 mM. Similarly, aqueous solutions of $HAuCl_4{\cdot}3H_2O$ with concentrations of ~12 mM and ~18 mM are prepared following the same procedure. Afterward, 20 ml $HAuCl_4$ solutions of three different concentrations are mixed with three individual 50 ml GO dispersed solutions dropwise. In these three individual mixture solutions, the weight ratio of GO and $HAuCl_4{\cdot}3H_2O$ is 1 : 1, 1 : 2, and 1 : 3, respectively. The resultant mixture solutions are stirred for 30 minutes at room temperature to allow interactions between the negatively charged oxygenated groups on GO and the $Au^{3+}$ ions from $HAuCl_4$. To reduce both the GO and the $Au^{3+}$ ions, a freshly prepared $NaBH_4$ solution (a strong reducing agent) is added dropwise to the mixture under ice-cold conditions with vigorous stirring. The reduction process is accompanied by a change in the color of the solution, indicating the reduction of $Au^{3+}$ to $Au^0$ and the simultaneous reduction of GO to rGO. The $NaBH_4$ reduction not only formed Au nanoparticles but also ensured that they are uniformly distributed over the rGO sheets.

Then, the mixture is transferred to a Teflon-lined stainless-steel autoclave and subjected to hydrothermal treatment. The autoclave is sealed and heated in an oven at 150 °C for 12 hours. The hydrothermal environment facilitated further reduction, crystallization of Au nanoparticles, and strong anchoring of the nanoparticles onto the rGO sheets, ensuring uniform heterostructure formation. After the hydrothermal reaction, the autoclave is allowed to cool naturally to room temperature. The product is collected by centrifugation and washed several times with DI water and ethanol to remove residual ions and impurities. The washed precipitate is then vacuum-dried at 60 °C for 12 hours to obtain the final rGO/Au heterostructure as a black powder.

### 2.3 Device fabrication process

The flexible memory devices are fabricated by using ITO-coated PET substrates. To ensure a clean and optimal surface for layer adhesion, the substrates underwent a thorough cleaning process. This involved sonication in deionized (DI) water, acetone, and isopropyl alcohol for 15 minutes each in an ultrasonic bath. After the wet cleaning, the substrates are treated with plasma for 10 minutes to increase their surface energy,

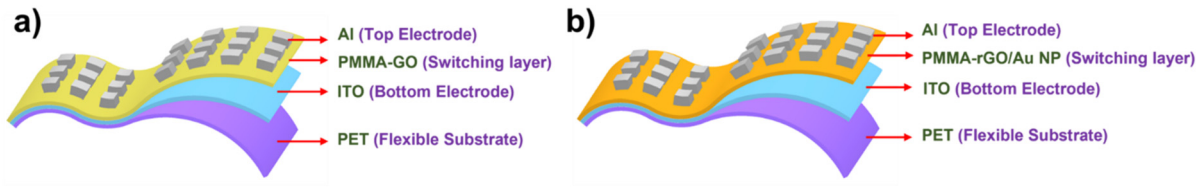


**Fig. 1** Schematic of the hierarchical architecture of PNC-based flexible devices. (a) D1 device with a PMMA-GO switching layer and (b) D2 device with a PMMA-rGO/Au NP switching layer.

enabling stronger adhesion to the subsequent nanocomposite layer.[34] A solution of the nanocomposite active material is then prepared and applied to the cleaned and treated substrates using a spin-coating technique. The spin coating is carried out at 1500 rpm for 60 seconds, resulting in a smooth and uniform film. Once coated, the substrates are placed in a vacuum oven and annealed at 70 °C for one hour. This step helped eliminate any residual solvents and improved the overall stability of the film. To complete the device fabrication, aluminum (Al) electrodes, 100 nm thick, are deposited onto the annealed films using thermal evaporation. These electrodes provided reliable electrical contact and finalized the device architecture. The fabrication process is carefully designed to ensure the creation of flexible devices with consistent performance and strong structural integrity. Fig. 1a and b illustrate the schematic layouts of the devices D1 and D2. This methodology set a solid foundation for subsequent electrical and mechanical evaluations, showcasing the potential of these devices for advanced memory applications.

### 2.4 Material characterization

A comprehensive suite of advanced characterization methods is employed to investigate the structural and morphological properties of the synthesized nanomaterials. Crystallographic phase identification is carried out using X-ray diffraction (XRD) analysis with a Rigaku Miniflex-600 diffractometer, enabling detailed phase determination and structural analysis. The nanoscale dimensions, morphology, and crystalline nature of the materials are analyzed using transmission electron microscopy (TEM, Tecnai G2 20). TEM provided high-resolution images, facilitating the observation of lattice structures and nanoparticle distribution. Microstructural surface features are examined using a scanning electron microscope (SEM, Zeiss), which offers insights into surface roughness, particle aggregation, and overall material uniformity. Fourier transform infrared (FTIR) spectroscopy is conducted in the spectral range of 400–4000 $cm^{-1}$ using a Nicolet iS5 spectrometer (THERMO Electron Scientific Instruments LLC), enabling the identification of functional groups and chemical bonding. Raman spectroscopy (WITec Alpha300 RAS) has been performed over the same spectral range to analyze vibrational modes and structural properties.

### 2.5 Electrical characterization of devices

The electrical performance of the fabricated devices is assessed through a series of cyclic current–voltage (*I–V*) measurements, along with endurance and retention tests. These evaluations are conducted using a semiconductor parameter analyzer (B1500, Keysight) to ensure precision and reliability. Two device configurations are analyzed in parallel to investigate their resistive switching behavior and to identify performance enhancements due to the incorporation of specific nanostructures. The first device, denoted as D1, consisted of a PET/ITO/(PMMA-GO)/Al structure that works as a reference device, whereas the second device, labeled as D2, employed a PET/ITO/(PMMA-rGO/Au)/Al configuration as the device of interest. In other words, D1 served as the reference to benchmark improvements achieved by the hybrid rGO/Au nanoparticle heterojunction in D2. This comparative approach provided critical insights into the impact of nanostructure engineering on the electrical characteristics of the devices, particularly in terms of operating voltage, current levels, switching stability, and data retention.

## 3. Results and discussion

### 3.1 Material characterization and surface morphological study

**3.1.1 XRD and Raman study.** The XRD pattern of GO exhibited a prominent diffraction peak at a $2\theta$ of ~10.2°, corresponding to the (001) plane of GO (Fig. S1a). This peak indicates an interlayer spacing of ~0.86 nm, which is significantly larger than that of pristine graphite (~0.34 nm). The increase in interlayer spacing arises due to the introduction of oxygen-containing functional groups (*e.g.*, hydroxyl, carboxyl, and epoxy groups) during the oxidation process, along with the intercalation of water molecules. The intensity and sharpness of the (001) peak signify the degree of oxidation and the structural ordering of GO sheets. The absence of a peak at a $2\theta$ of ~26°, characteristic of the (002) plane of graphite, confirms the effective exfoliation of graphite into GO sheets. A broad and intense diffraction peak appears at a $2\theta$ of ~26°, corresponding to the (002) plane of rGO. This shift signifies a decrease in interlayer spacing (~0.34 nm), attributed to the restoration of $sp^2$ hybridized carbon domains and partial recovery of graphene's π–π stacking interactions. Sharp and intense diffraction peaks are observed at $2\theta$ of ~38°, 44°, and 64° corresponding to the (111), (200), and (220) planes of face-centered cubic (fcc) gold, respectively (JCPDS no. 04-0784). These peaks confirm the crystalline nature of the Au nanoparticles in the heterostructure (Fig. 2a). The high intensity and narrow

 

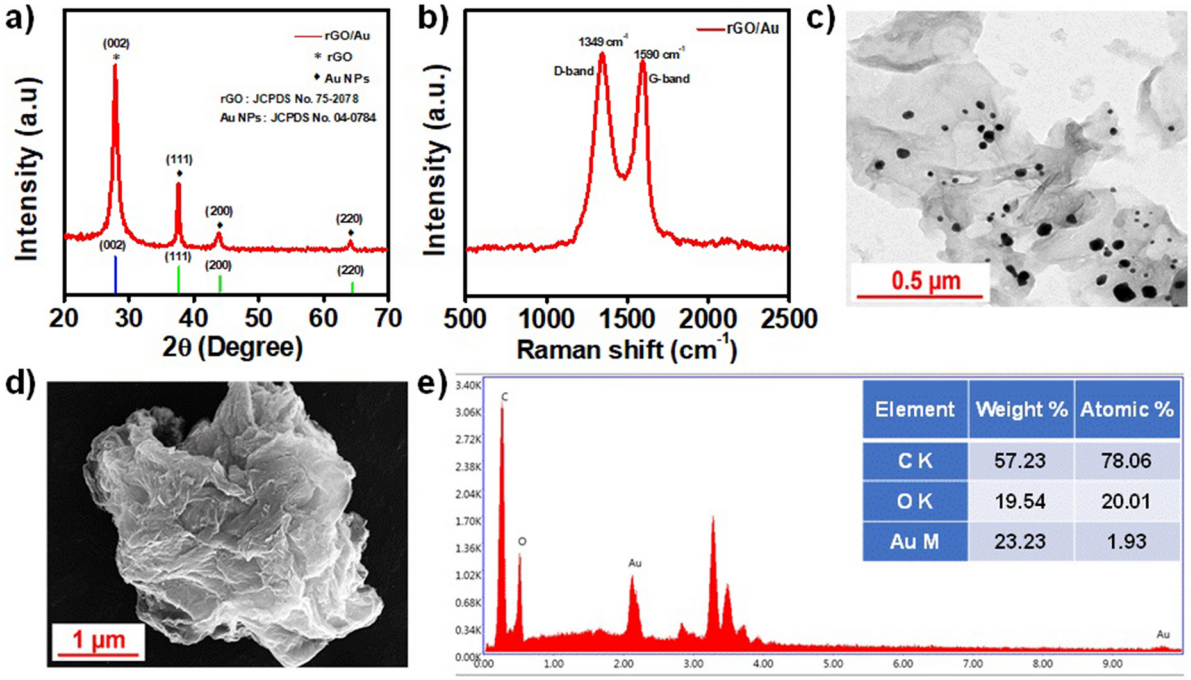


**Fig. 2** (a) XRD spectra; (b) Raman spectrum of rGO/Au; (c) high-resolution TEM image of rGO/Au; (d) high-resolution SEM image of rGO/Au; and (e) EDX analysis corresponding to the HRSEM image.

width of the (111) peak indicate the preferential growth of Au nanoparticles along this plane, a common observation in gold nanostructures due to their lower surface energy.

The Raman spectrum of GO is characterized by two primary peaks. The D-band (~1350 $cm^{-1}$) originates from the breathing modes of $sp^2$ carbon atoms in the presence of structural defects and disorder. Its intensity is relatively high due to the disruption of the $sp^2$ network caused by oxygen-containing functional groups and defects introduced during oxidation. The G-band (~1585 $cm^{-1}$) corresponds to the in-plane vibration of $sp^2$-bonded carbon atoms. It is slightly broadened and downshifted compared to pristine graphene, reflecting the reduction in graphitic domain size and the introduction of functional groups (Fig. S1b). The Raman spectrum of rGO/Au exhibits notable changes compared to GO, indicative of the reduction process and the incorporation of gold nanoparticles. The position of the D-band remains nearly unchanged, but its intensity may increase slightly due to residual defects in rGO after the reduction process. The G-band shifts upward slightly and becomes sharper, reflecting the partial restoration of the $sp^2$-hybridized carbon network during the reduction of GO to rGO (Fig. 2b). The interaction of Au nanoparticles with rGO does not introduce new Raman features but enhances the signal intensity *via* SERS. This suggests strong coupling between the Au nanoparticles and the rGO surface, crucial for the heterostructure's electrical and chemical performance. The FTIR spectrum of GO shows peaks at ~3200–3400 $cm^{-1}$ (–OH), ~1645 $cm^{-1}$ (C═O), ~1356 $cm^{-1}$ (C–O–C), and ~1050 $cm^{-1}$ (C–O), which are greatly reduced in the rGO/Au heterostructure, while a new peak at ~1563 $cm^{-1}$ (C═C) confirms oxygen group removal and $sp^2$ carbon restoration; detailed analysis is provided in section S1 (Fig. S2).

**3.1.2 Surface morphology study through FESEM and HRTEM.** GO exhibits a layered, sheet-like morphology with wrinkled and crumpled surfaces (Fig. S3a). This morphology arises from the exfoliation of graphite into individual or few-layered GO sheets during the oxidation process. The wrinkles and folds are primarily due to van der Waals interactions between adjacent sheets and the stress induced by oxygen-containing functional groups. The reduction of GO to rGO results in a more distinct, layered morphology with fewer wrinkles and folds. This change is attributed to the partial removal of oxygen functional groups and the restoration of the $sp^2$ network, enhancing structural integrity. The sheets appear more interconnected, reflecting improved electrical conductivity due to the restoration of π–π stacking interactions. Spherical Au nanoparticles are observed to be uniformly distributed on the rGO sheets (Fig. 2d). The chemical composition of the C, O, and Au components within the rGO/Au heterostructure is confirmed using an energy-dispersive X-ray (EDX) spectrometer connected to an HR-SEM analyzer (Fig. 2e). Fig. S4 depicts a color map of the rGO/Au heterostructure, highlighting the homogeneous distribution of C, O, and Au across the films.

The HRTEM images of GO (Fig. S3b) show ultrathin, transparent sheets with lateral dimensions of several micrometers, confirming successful exfoliation into individual or few-layered nanosheets. Pronounced wrinkles and folds arise from mechanical stress during exfoliation and interactions between oxygen functional groups and water molecules, which enhance

the surface area and flexibility of GO. After reduction, rGO retains some wrinkles but exhibits a more planar structure. To investigate the effect of Au nanoparticle size and concentration, rGO/Au heterostructures are synthesized at three different GO : $HAuCl_4 \cdot 3H_2O$ weight ratios (1 : 1, 1 : 2, and 1 : 3). Among them, the 1 : 1 weight ratio ensures uniform nucleation and anchoring of Au nanoparticles (~10–20 nm) on rGO sheets, resulting in homogeneous dispersion without noticeable agglomeration (Fig. 2c). At higher Au loadings (1 : 2 and 1 : 3), uncontrolled nanoparticle growth and aggregation occur, leading to non-uniform surface decoration and disruption of effective conductive pathways. The comparative HRTEM images for these ratios are provided in Fig. S5 of the SI. These results confirm that the synthesis approach provides precise control over Au nanoparticle size distribution by adjusting the GO : Au ratio. Among the studied compositions, the 1 : 1 ratio yields uniformly dispersed nanoparticles, strong interfacial contact, and enhanced electronic coupling between Au and rGO, which are crucial for efficient charge transport. To further optimize device performance, different rGO/Au loadings (0.1–1 wt%) are incorporated into the PMMA matrix. The highest current ON/OFF ratio is obtained at a 0.5 wt% loading, which is selected as the optimal composition for device fabrication and subsequent electrical characterization. The thickness of the PMMA-rGO/Au active layer is measured using AFM height profile analysis, revealing an average thickness of ~460 nm. The AFM scans recorded in multiple regions indicate a thickness variation of less than ±4%, confirming good uniformity across the substrate (Fig. S6).

### 3.2 Electrical characterization of memristor devices

**3.2.1 Bistable memory operation.** The memory switching behaviors of D1 and D2 devices are analyzed under reversible voltage bias, as shown in Fig. 3a and d, respectively. For D1, the investigation involved a voltage sweep from −4 V to +4 V,

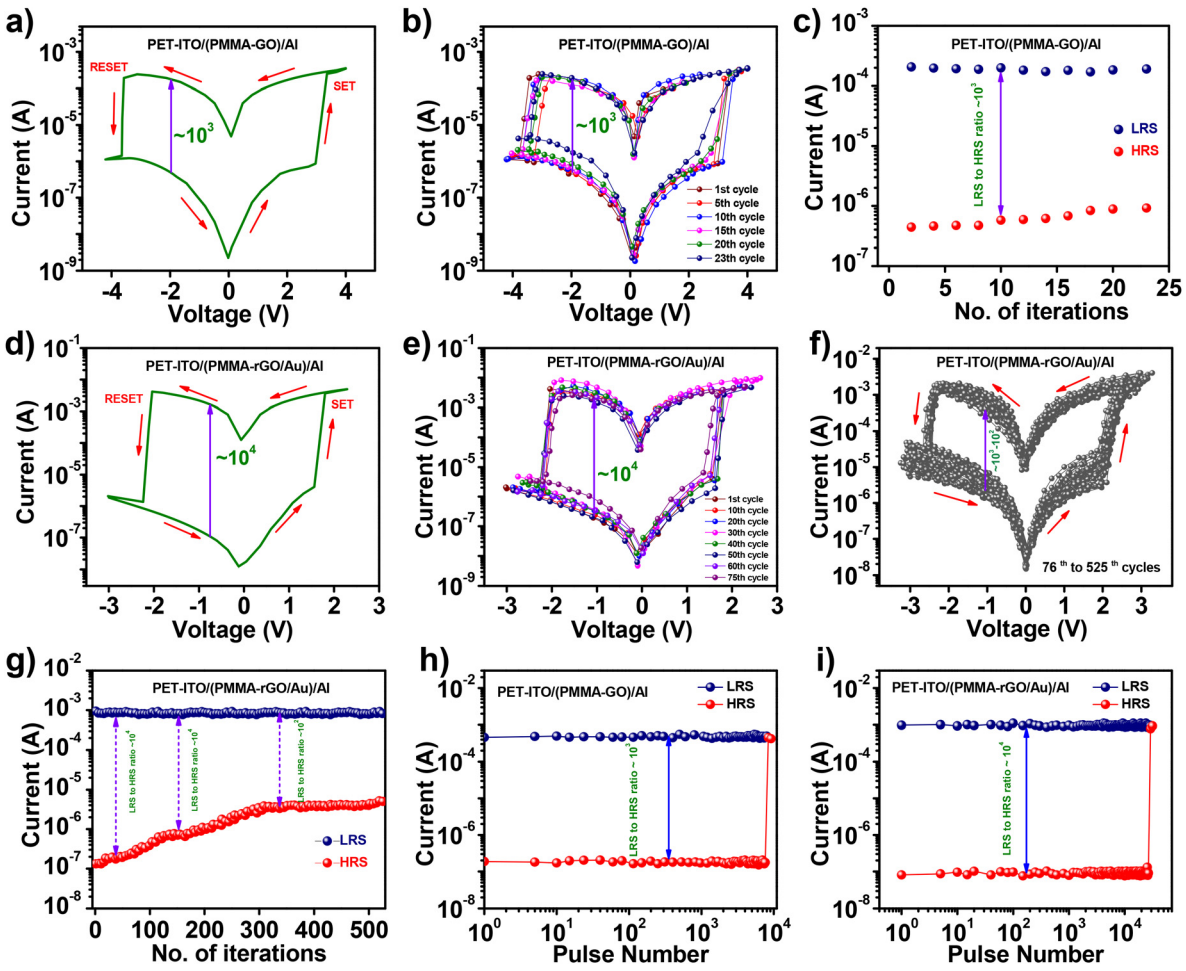


Fig. 3 (a and d) Semi-logarithmic plot of current *vs.* voltage for PET-ITO/(PMMA-GO)/Al and PET-ITO/(PMMA-rGO/Au)/Al for a single cycle; (b and e) current *vs.* voltage graph of PET-ITO/(PMMA-GO)/Al and PET-ITO/(PMMA-rGO/Au)/Al on a semi-logarithmic scale for multiple sweeps; (c and g) endurance properties of PET-ITO/(PMMA-GO)/Al and PET-ITO/(PMMA-rGO/Au)/Al; (f) current *vs.* voltage graph of PET-ITO/(PMMA-rGO/Au)/Al on a semi-logarithmic scale from the 76$^{th}$ to the 525$^{th}$ cycles; and (h and i) pulse endurance measurement of PET-ITO/(PMMA-GO)/Al and PET-ITO/(PMMA-rGO/Au)/Al.

performed under ambient conditions. A compliance current of 10 mA is used to safeguard the device against electrical damage. During the positive voltage sweep, the D1 device initially exhibited a high-resistance state (HRS), indicating minimal current flow. However, upon reaching a threshold voltage of +2.9 V, the resistance dropped sharply, marking a transition to the low-resistance state (LRS). This abrupt change, identified as the SET operation, corresponds to the process of writing data into the memory device. Importantly, the device retained the LRS after the removal of the external bias, confirming its non-volatile nature. Conversely, during the subsequent negative voltage sweep, a RESET operation was observed. At a critical voltage of −3.25 V, the device switched back from the LRS to the HRS, effectively erasing the stored data. Successive cycles of negative and positive sweeps demonstrated stable and repeatable switching, underscoring the rewritable nature of D1. The ratio of currents in the ON and OFF states for D1 is found to be approximately $10^3$. D2, utilizing a reduced graphene oxide (rGO)/gold (Au) nanoparticle hybrid as the active layer, exhibited superior performance at reduced voltages compared to D1. For D2, a lower voltage range of −3 V to +3 V is applied, maintaining the same compliance current. The device, initially in its HRS, transitioned to the LRS at a SET voltage of +1.4 V during the positive sweep. This lower switching voltage is indicative of the enhanced electrical properties of the rGO/Au nanocomposite. The LRS persisted after bias removal, demonstrating reliable data retention. Upon applying a negative voltage sweep, the D2 device underwent RESET at −2.15 V, reverting to the HRS. The reversible switching is further confirmed by repeating write–read–erase cycles, highlighting the device's suitability for non-volatile memory applications. Remarkably, the D2 device achieved an ON-to-OFF ratio of approximately $10^4$, exceeding that of D1.

The enhanced characteristics of D2 arise from the distinctive properties of the rGO/Au heterostructure. Reduction of graphene oxide to rGO restores the conductive graphitic domains, ensuring efficient charge transfer. The presence of Au nanoparticles introduces localized electronic states, acting as active sites for charge storage and improving overall conductivity. Furthermore, the nanoscale interaction between rGO sheets and Au nanoparticles facilitates better charge mobility and reduced energy barriers, contributing to lower operating voltages and enhanced switching stability. The unique combination of rGO and Au in D2 not only reduces energy consumption but also provides superior data retention and endurance, establishing this device as a highly promising candidate for next-generation non-volatile memory technologies.

**3.2.2 Endurance and retention characteristics.** Endurance analysis evaluates the device's switching cycle limit before notable performance degradation. Fig. 3b, e, and f display the *I–V* characteristics of devices D1 and D2 over multiple switching cycles. Device D1 exhibits stable resistive switching for approximately 25 cycles, maintaining a LRS to HRS ratio of $\sim 10^3$. In comparison, the heterostructure-based device D2 demonstrates enhanced endurance, sustaining consistent performance for 75 cycles with an LRS to HRS ratio of $\sim 10^4$. Beyond this, although device D2 experiences a gradual degradation in the LRS to HRS ratio after 75 cycles, it continues to operate within a stable switching range up to 525 cycles. A one-order magnitude difference between the LRS and the HRS is observed up to 230 cycles, while a two-order magnitude variation persists up to 525 cycles. Even after 525 cycles, D2 continues to exhibit reliable switching behavior. The current levels in both the HRS and the LRS are continuously monitored over time to verify the operational stability of the devices, as shown in Fig. 3c and g. To further assess durability under repetitive electrical stress, pulse endurance tests are performed. Device D1 maintains stable switching characteristics for approximately $10^4$ pulse cycles, while device D2 retains its performance up to $\sim 10^5$ cycles, confirming its superior robustness and long-term reliability. The corresponding pulse endurance results for devices D1 and D2 are illustrated in Fig. 3h and i.

Retention time analysis assesses how long the device maintains its LRS or HRS after removing the external bias. Before this, a fixed voltage is applied to the device for 60 seconds. Fig. 4a and b show the retention behavior of the D1 and D2 devices. From this analysis, it is observed that in the case of the D1 device, its HRS (OFF state) degraded after $10^2$ s, while its LRS (ON state) remained stable for the same duration. Alternatively, the D2 device demonstrated excellent retention, with the LRS remaining stable for over $10^4$ s, while the HRS showed only slight degradation after $10^4$ s. To the best of our knowledge, this value is one of the highest reported retention times among solution-processed flexible memristor devices.[35–37] To evaluate the thermal stability and reliable performance of the devices, additional retention measurements have been performed at an elevated temperature of 85 °C. The results, provided in Fig. S7, show that both the ON/OFF current ratio and the retention time exhibit only a negligible reduction compared to room-temperature measurements, confirming the robustness of device performance under elevated-temperature conditions. The incorporation of Au NPs between the rGO nanosheets during heterostructure formation reduces surface defects and structural instability, allowing the D2 device to maintain its HRS and LRS for extended periods, which is the key novelty of this work. Moreover, the formation of a stable Schottky junction at the rGO/Au NP interface further improves interfacial modulation, enhancing cycling and retention stability.

We conducted a statistical analysis to examine the average set and reset voltages of the memristor device (Fig. 4d & e). Following Gaussian fitting, we observed that the average set voltage is +1.80 V, and the average reset voltage is −1.81 V. To evaluate device-to-device variation, we measured the LRS/HRS ratio and switching voltage distribution for 25 different devices (Fig. 4c & f). The results showed that the LRS/HRS ratio for all devices is approximately $10^3$, and the average set and reset voltages are around +1.8 V and −1.8 V, respectively. This confirms the overall consistency of the switching behavior across multiple cycles and devices.

**3.2.3 Flexibility study.** A flexible study is performed in order to evaluate the flexibility performance of the D2 device. Fig. 5a displays a digital image of the fabricated flexible device

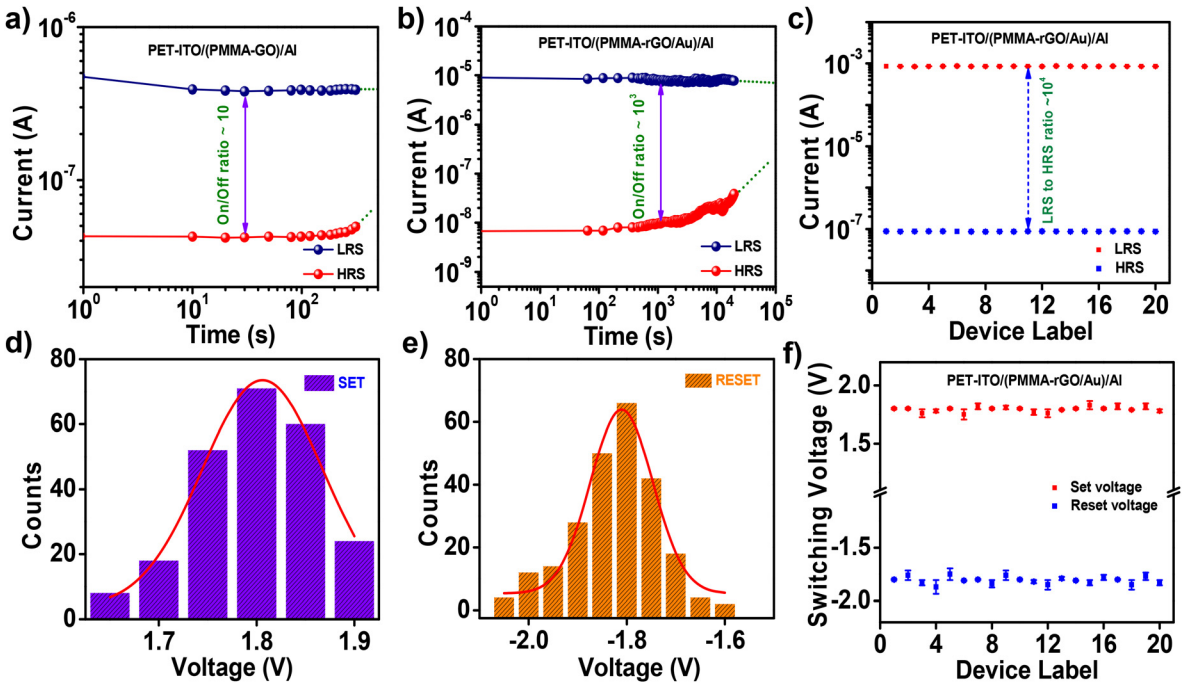


**Fig. 4** Retention time measurement of (a) PET-ITO/(PMMA-GO)/Al and (b) PET-ITO/(PMMA-rGO/Au)/Al, respectively; (c) device-to-device variation of LRS and HRS distributions; (d and e) the statistical histograms of set and reset voltages over 525 consecutive cycles of PET-ITO/(PMMA-rGO/Au)/Al; and (f) device-to-device variation of switching voltage.

along with the bending apparatus. The *I*–*V* characteristics are measured for both the flat configuration and under different bending stresses, as shown in Fig. 5b, and the corresponding current values of the HRS and the LRS are provided in Fig. 5c. The characteristics are evaluated at bending radii of 10 mm, 8 mm, 6 mm, and 5 mm, with the device maintaining excellent electrical performance even at a critical radius of 6 mm. The device showed an $I_{ON}/I_{OFF}$ ratio of $\sim 10^4$ with operating voltages within −2 V to +2 V. However, bending beyond the 6 mm critical radius caused significant degradation due to mechanical damage to the active layer and electrode disintegration. This is indicated by a significant drop in the $I_{ON}/I_{OFF}$ ratio by over $10^3$ and a shift in the threshold voltage beyond the −2.5 V operating range. The flexibility performance is further evaluated by examining the device's bending endurance. A bending radius of 10 mm is maintained throughout this experiment. The current values in both the HRS and the LRS are measured after every 100 bending cycles to assess the electrical stability of the flexible device under repeated mechanical stress. The results of the bending endurance of the D2 device are shown in Fig. 5d. The HRS and LRS current values showed that the device maintained stable electrical characteristics even after 1000 continuous bending cycles, confirming its suitability for flexible, portable electronics. The flexibility and electrical performance of this work are compared to recently published studies, as provided in (Table 1).

Furthermore, the *I*–*V* characteristics of the D2 device are analyzed on a double logarithmic scale to clarify the conduction mechanism in both the LRS and HRS. In the positive sweep region, the LRS or ON state exhibits ohmic behavior (region IV), characterized by a linear dependence on the applied bias with a slope of approximately 1.11. The formation of a conductive pathway between the top and bottom electrodes through the FN tunneling process enables the device to function as an ohmic conductor. The HRS or OFF state is divided into three distinct regions. In region I, ohmic conduction is observed at low applied voltages because the bias is too weak to induce electron de-trapping from the charge trapping centers. As a result, the current shows a linear relationship with voltage, with a slope of approximately 1.20. Region II, a relatively smaller region, follows the Mott–Gurney law for semiconductors, where free charge carriers drift at a velocity $v = \mu \times e$ ($\mu$ is the mobility of electrons and $e$ is the charge of an electron), and the current density is proportional to the square of the applied voltage ($I \sim V^2$). The slope derived from the *I*–*V* characteristics in region II closely aligns with a value of approximately 2.42 reflecting the space-charge-limited current (SCLC) mechanism due to the Schottky junction formation in the composite active layer and electrode interfaces. Region III shows a sharp rise in current relative to a small change in applied bias. The current follows the relationship $I = V^{\alpha}$, where $\alpha$ is approximately 47.72, which is due to the very high energy gained by the trapped carrier to escape the barrier, resulting in very large variation of current with a very small variation of external bias (Fig. 5e). In the negative sweep region, both the LRS and the HRS follow the same pattern. The slope values of region I, region II, region III, and region IV are 1.03, 2.34, 48.6, and 1.04, respectively (Fig. 5f).

 

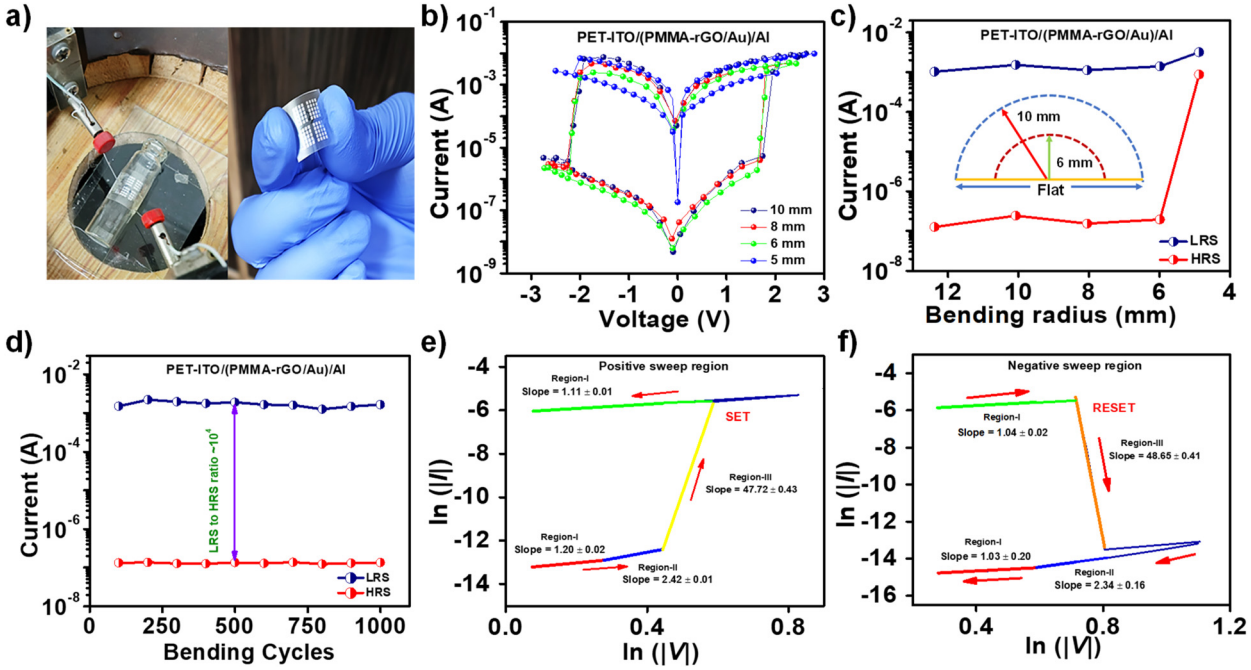


**Fig. 5** (a) Digital image of the fabricated flexible device and the bending apparatus; (b) semi-log plot of *I*–*V* characteristics of the PET-ITO/(PMMA-rGO/Au)/Al device under different bending radii; (c) current levels of the PET-ITO/(PMMA-rGO/Au)/Al device in the HRS and LRS without bending and under different bending radii; (d) current values of the PET-ITO/(PMMA-rGO/Au)/Al device in the HRS and LRS after multiple bending cycles; and *I*–*V* characteristics of the PET-ITO/(PMMA-rGO/Au)/Al device on a double logarithmic scale illustrating the conduction mechanism in both the HRS and the LRS in (e) the positive sweep region and (f) the negative sweep region.

**Table 1** Comparison of the flexibility and electrical performance of this work with recently published studies

| Device configuration | On/off ratio | Cyclic endurance | Pulse endurance | Retention | Bending radius (mm) | Bending cycles | Ref. |
|---|---|---|---|---|---|---|---|
| PET/ITO/AuNPs-RGO PVA/Al | $10^3$ | 25 | — | $10^3$ | — | — | 33 |
| PET/ITO/$Ti_3C_2T_x$-PVA/Ag | 10 | 50 | — | ~$10^4$ | — | 100 | 38 |
| PET/ITO/DUV-ZnO/Ag | ~$10^2$ | 120 | — | $10^3$ | 8 | >1000 | 39 |
| PET/Au/Au-chitosan/Ag | 10 | 100 | — | $10^4$ | 5 | 800 | 40 |
| PET/ITO/(PMMA-rGO/Au NP)/Al | ~$10^4$<br>~$10^3$<br>~$10^2$ | 75<br>76 to 230<br>231 to 525 | ~$10^5$ | >$10^4$ | 6 | 1000 | This work |

**3.2.4 Resistive switching model and conduction mechanism.** The reversible switching of D2 is driven by bias-dependent band bending, charge carrier modulation in rGO/Au NP, and transport to the electrode. Fig. 6a shows the energy band diagram of the D2 device (PET/ITO/(PMMA-rGO/Au NP)/Al) in the HRS under zero bias. Accordingly, a close-up view of the energy band diagram for PMMA-rGO/Au NP is provided in Fig. 6b. Under the application of a negative voltage to the top electrode (Al electrode), electrons are transferred through the PMMA layer to the LUMO level of rGO/Au NP *via* FN tunneling. Due to the higher electron affinity of rGO/Au NP (4.75 eV) in comparison with the LUMO level of PMMA (1.65 eV), rGO/Au acts as an electron trapping and transport layer. Furthermore, gold (Au) exhibits a higher electron affinity of 5.1 eV and a broad band gap of 2.7 eV, as determined from UV-Vis absorption data, which significantly improves the charge-trapping properties of the active layer.

PMMA acts as a hole-blocking layer, preventing hole migration from ITO to the active layer due to the large energy gap between the work function of ITO (4.8 eV) and the HOMO level of PMMA (7.25 eV). Additionally, PMMA's wider band gap (5.6 eV) reduces carrier recombination in the active layer and supports electron accumulation at the charge-trapping centers (Fig. 6c). This charge-trapping phenomenon persists until the rGO/Au NP layer reaches its maximum capacity. Additionally, increasing the external bias saturates this capacity, leading to the formation of a conductive pathway, known as the conducting filament, between the top Al and bottom ITO electrodes. The formation of a dense conductive filament switches the device from the HRS (OFF) to the LRS (ON) *via* the space-charge-limited current (SCLC) mechanism,

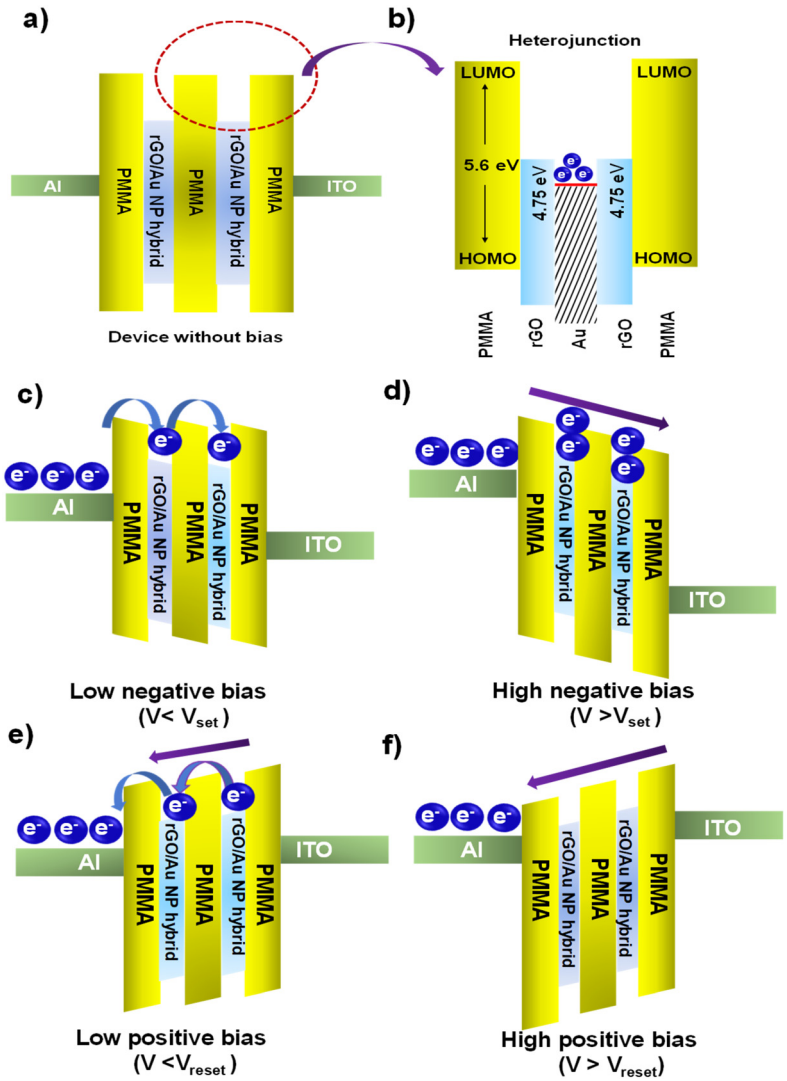


**Fig. 6** Band diagram of the PET-ITO/(PMMA-rGO/Au)/Al device to illustrate the carrier mechanism: (a) energy band with zero bias; (b) close-up view of PMMA/(rGO/Au NP)/PMMA; (c) device under low negative bias; (d) device under high negative bias; (e) device under low positive bias; and (f) device under high positive bias.

representing the SET (writing) process (Fig. 6d). The PMMA/(rGO/Au NP)/PMMA network retains trapped electrons after bias removal, enabling storage. On the other hand, upon the application of positive voltage, initially, the LRS (ON) state is maintained until a specific external bias is reached ($V < V_{reset}$) (Fig. 6e). In this step, trapped electrons are gradually released while the device remains in the LRS (ON) state. However, the switch from the LRS to the HRS occurs only after applying a sufficient positive bias, which removes most of the trapped electrons from the rGO/Au NP layer. Upon applying $V_{reset}$, electrons are de-trapped and returned to the top Al electrode through the FN tunneling process, causing the device to switch back to the HRS (OFF state) (Fig. 6f). Thus, the trap-controlled SCLC mechanism and FN tunneling operate cyclically, imparting unique non-volatile bistable memory characteristics to the rGO/Au NP heterostructure-based device.

## 4. Conclusion

This study demonstrated the fabrication and performance of flexible memristor devices based on PMMA-embedded graphene and gold nanoparticle heterostructures. The innovative combination of reduced graphene oxide (rGO) and gold nanoparticles (Au NPs) within the polymer matrix has significantly improved device stability, reduces operating voltage, and increases retention capability. We established through detailed structural and electrical analyses that the unique synergy between rGO and Au NPs enhances charge transport, reduces energy barriers, and promotes stable resistive switching behavior. Compared to the reference device, which utilized GO without Au nanoparticles, the proposed rGO/Au nanocomposite system exhibited lower operating voltages, a higher ON/OFF current ratio, and remarkable retention characteristics

 

with a retention time of $\sim 2 \times 10^4$ s. The transformation of GO to rGO effectively restored electrical conductivity, while the presence of gold nanoparticles added localized states that facilitated efficient charge trapping and release, contributing to improved switching stability and endurance. The flexible design of these memristors, enabled by the use of PET substrates, aligns with the growing demand for next-generation memory devices that combine durability, performance, and adaptability for wearable electronics and other portable applications. The demonstrated advancements in performance, including enhanced stability and high retention times, position these memristors as promising candidates for future developments in flexible, non-volatile memory technologies.

## Conflicts of interest

The authors explicitly state that they have no conflicts of interest to disclose, ensuring that their work remains impartial and free from any potential biases or external influences.

## Data availability

The data supporting this article have been included as part of the supplementary information (SI). Supplementary information: XRD and Raman spectra of GO are provided in Fig. S1; FTIR analysis results of GO and rGO/Au heterostructure are provided in Fig. S2; high-resolution SEM and TEM images of GO are provided in Fig. S3; the color map of the rGO/Au heterostructure is provided in Fig. S4; HR-TEM images of rGO/Au heterostructures synthesized with different GO : Au molar ratios are given in Fig. S5; the AFM image of the scratched PMMA-rGO/Au film and its line-scan height profile are presented in Fig. S6; retention time measurements at an elevated temperature of 85 °C are shown in Fig. S7; and detailed FTIR analysis results of GO and rGO/Au NP heterostructures are discussed in section S1. See DOI: **https://doi.org/10.1039/d5nr02726h**.

## Acknowledgements

Bhola Nath Pal thanks SERB, India (CRG/2019/001826) and DST, India (DST/INT/SWD/VR/P-12/2019) for financial support. Dr B. N. Pal also acknowledges the financial support from the Center for Energy & Resources Development (CERD), IIT (BHU). The authors are grateful to the Central Instrument Facility Centre, IIT (BHU) for providing the FE-SEM, HR-TEM, and XRD measurement facilities. The authors also acknowledge the Central Discovery Centre, Banaras Hindu University, for providing Raman analysis facilities. Shivam Awasthi and Rajarshi Chakraborty thank IIT (BHU) for providing PhD fellowships. Subarna Pramanik acknowledges DST, India, for providing a PhD fellowship.

## References

1 R. Chakraborty, S. Pramanik, N. Pal, U. Pandey, S. Suman, P. Swaminathan and B. N. Pal, *ACS Appl. Mater. Interfaces*, 2024, **16**, 47820–47831.
2 R. Chakraborty, N. Pal, U. Pandey, S. Pramanik, S. Paliwal, S. Suman, A. Gupta, A. K. Singh, P. Swaminathan and P. K. Roy, *Appl. Mater. Today*, 2023, **33**, 101862.
3 J. J. Qin, B. Sun, G. D. Zhou, T. Guo, Y. Z. Chen, C. Ke, S. S. Mao, X. L. Chen, J. Y. Shao and Y. Zhao, *ACS Mater. Lett.*, 2023, **5**, 2197–2215.
4 S. Pramanik, R. Chakraborty, S. Hazra, U. Pandey and B. N. Pal, *J. Mater. Chem. C*, 2024, **12**, 16145–16155.
5 M. A. Lastras-Montaño and K. T. Cheng, *Nat. Electron.*, 2018, **1**, 466–472.
6 K. J. Kwak, D. E. Lee, S. J. Kim and H. W. Jang, *J. Phys. Chem. Lett.*, 2021, **12**, 8999–9010.
7 S. S. T. Nibhanupudi, A. Roy, D. Veksler, M. Coupin, K. C. Matthews, M. Disiena, J. V. Singh, I. R. Gearba-Dolocan, J. Warner, J. P. Kulkarni, G. Bersuker and S. K. Banerjee, *Nat. Commun.*, 2024, **15**, 2334.
8 T. Wang, Z. Q. Cui, Y. Q. Liu, D. J. Lu, M. Wang, C. J. Wan, W. R. Leow, C. X. Wang, L. Pan, X. Cao, Y. Z. Huang, Z. J. Liu, A. L. Y. Tok and X. D. Chen, *Adv. Mater.*, 2022, **34**, 2106212.
9 S. Q. Cheng, L. Zhong, J. X. Yin, H. Duan, Q. Xie, W. B. Luo and W. J. Jie, *Nanoscale*, 2023, **15**, 4801–4808.
10 R. Yuan, P. J. Tiw, L. Cai, Z. Y. Yang, C. Liu, T. Zhang, C. Ge, R. Huang and Y. C. Yang, *Nat. Commun.*, 2023, **14**, 3695.
11 Z. Yang, X. Huang, Y. Liu, Z. Wang, Z. Zhang, B. Ma, H. Shang, L. Wang, T. Zhu, X. Duan, H. Hu and J. Yue, *Small Methods*, 2024, **9**, 2401259.
12 J. Yue, L. Zou, N. Bai, C. Zhu, Y. Yi, F. Xue, H. Sun, S. Hu, W. Cheng, Q. He, H. Lu, L. Ye and X. Miao, *Small Methods*, 2024, **8**, 2301657.
13 H. Duan, S. Q. Cheng, L. Qin, X. L. Zhang, B. Y. Xie, Y. Zhang and W. J. Jie, *J. Phys. Chem. Lett.*, 2022, **13**, 7130–7138.
14 Z. L. Dong, Q. L. Hua, J. G. Xi, Y. H. Shi, T. C. Huang, X. H. Dai, J. A. Niu, B. J. Wang, Z. L. Wang and W. G. Hu, *Nano Lett.*, 2023, **23**, 3842–3850.
15 S. Dahiya, U. Pandey, S. Hazra, R. Chakraborty, S. Pramanik, P. P. Maurya and B. N. Pal, *Adv. Mater. Technol.*, 2025, **10**, 2401532.
16 S. Dahiya, S. Hazra, U. Pandey, S. Pramanik, P. Dahiya, S. V. Singh, N. Kumari and B. N. Pal, *Opt. Mater.*, 2024, **157**, 116182.
17 P. K. Aich, Z. Genene, U. Pandey, A. K. Yadav, E. Wang and B. N. Pal, *ACS Photonics*, 2024, **11**, 3704–3712.
18 S. Hazra, S. Dahiya, S. V. Singh, U. Pandey, S. Suman, P. Swaminathan and B. N. Pal, *Chem. Eng. J.*, 2024, **498**, 155313.
19 D. W. Tao, Z. J. Jiang, J. B. Chen, B. J. Qi, K. Zhang and C. W. Wang, *Appl. Surf. Sci.*, 2021, **539**, 148161.

20 J. Q. Chen, X. Q. Liu, C. Liu, L. Tang, T. Bu, B. Jiang, Y. H. Qing, Y. L. Xie, Y. Wang, Y. T. Shan, R. X. Li, C. Ye and L. Liao, *Nano Lett.*, 2024, **24**, 5371–5378.
21 D. Lee, S.-M. Kim, J.-C. Park, Y. Jung, S. Lee, B. H. Lee and S. Lee, *Appl. Surf. Sci.*, 2025, **679**, 161216.
22 T. Dehury, S. Kumar, S. Pütter, S. Roy, S. Sahoo and C. Rath, *Appl. Surf. Sci.*, 2025, **685**, 162060.
23 M. Ismail, M. Rasheed, Y. Park, J. Lee, C. Mahata and S. Kim, *Nanoscale*, 2025, **17**, 361–377.
24 Y. Wang, W. Duan, J. Meng, W. Zhang, Z. Liu, D. Guo, Z. Lv, J. Yu and H. Guan, *J. Mater. Chem. C*, 2025, **13**, 5920–5928.
25 S. Pramanik, R. Chakraborty, S. Hazra, P. P. Maurya, C. Pan and B. N. Pal, *ACS Appl. Nano Mater.*, 2025, **8**, 14972–14982.
26 H. L. Park, M. H. Kim, H. Kim and S. H. Lee, *Adv. Electron. Mater.*, 2021, **7**, 2100299.
27 L. Han, D. H. Wang, M. D. Li, Y. Zhong, K. H. Liao, Y. B. Shi and W. J. Jie, *Carbon*, 2024, **218**, 118665.
28 X. N. Zhao, Z. Q. Wang, W. T. Li, S. W. Sun, H. Y. Xu, P. Zhou, J. Q. Xu, Y. Lin and Y. C. Liu, *Adv. Funct. Mater.*, 2020, **30**, 1910151.
29 C. Liu, Y. Q. Cao, D. Wu and A. D. Li, *IEEE Electron Device Lett.*, 2020, **41**, 155–158.
30 D. Panda, Y.-F. Hui and T.-Y. Tseng, *Nanoscale*, 2024, **16**, 16148–16158.
31 B. Walters, M. V. Jacob, A. Amirsoleimani and M. R. Azghadi, *Adv. Intell. Syst.*, 2023, **5**, 2300136.
32 A. H. Jaafar, L. C. Meng, T. J. Zhang, D. K. Guo, D. Newbrook, W. J. Zhang, G. Reid, C. H. de Groot, P. N. Bartlett and R. M. Huang, *ACS Appl. Nano Mater.*, 2022, **5**, 17711–17720.
33 A. Midya, N. Gogurla and S. K. Ray, *Curr. Appl. Phys.*, 2015, **15**, 706–710.
34 S. Hazra, S. Dahiya, J. P. Bijarniya, S. Pramanik, J. Sarkar and B. N. Pal, *ACS Appl. Energy Mater.*, 2024, **7**, 7316–7324.
35 J. Ren, H. Liang, J. Li, Y. C. Li, W. Mi, L. Zhou, Z. Sun, S. Xue, G. Cai and J. S. Zhao, *ACS Appl. Mater. Interfaces*, 2022, **14**, 14541–14549.
36 Z. Zhou, F. Xiu, T. Jiang, J. Xu, J. Chen, J. Liu and W. Huang, *J. Mater. Chem. C*, 2019, **7**, 10764–10768.
37 Z. Zhou, H. Mao, X. Wang, T. Sun, Q. Chang, Y. Chen, F. Xiu, Z. Liu, J. Liu and W. Huang, *Nanoscale*, 2018, **10**, 14824–14829.
38 S. Ling, C. Zhang, C. Zhang, M. Teng, C. Ma, J. Gao, X. Yan, Y. Pan, Y. Jiang and Y. Wu, *J. Solid State Chem.*, 2023, **318**, 123731.
39 X. Wu, Z. Xu, Z. Yu, T. Zhang, F. Zhao, T. Sun, Z. Ma, Z. Li and S. Wang, *J. Phys. D: Appl. Phys.*, 2015, **48**, 115101.
40 N. Raeis-Hosseini and J. Rho, *ACS Appl. Mater. Interfaces*, 2021, **13**, 5445–5450.